Chemical Science

ROYAL SOCIETY OF CHEMISTRY

EDGE ARTICLE

View Article Online
View Journal | View Issue

Cite this: *Chem. Sci.*, 2020, **11**, 7708

All publication charges for this article have been paid for by the Royal Society of Chemistry

Dimensional reduction of the small-bandgap double perovskite $Cs_2AgTlBr_6$†

Bridget A. Connor, [a] Raisa-Ioana Biega,[b] Linn Leppert [*b] and Hemamala I. Karunadasa [*ac]

Quantum confinement effects in lower-dimensional derivatives of the ABX_3 (A = monocation, X = halide) single perovskites afford striking optical and electronic changes, enabling applications ranging from solar absorbers to phosphors and light-emitting diodes. Halide double perovskites form a larger materials family, known since the late 1800s, but lower-dimensional derivatives remain rare and prior work has revealed a minimal effect of quantum confinement on their optical properties. Here, we synthesize three new lower-dimensional derivatives of the 3D double perovskite $Cs_2AgTlBr_6$: 2D derivatives with mono- (**1-Tl**) and bi-layer thick (**2-Tl**) inorganic sheets and a quasi-1D derivative (**1'-Tl**). Single-crystal ellipsometry studies of these materials show the first clear demonstration that dimensional reduction can significantly alter the optical properties of 2D halide double perovskites. This large quantum confinement effect is attributed to the substantial electronic delocalization of the parent 3D Ag–Tl perovskite. Calculations track the evolution of the electronic bands with dimensional reduction and the accompanying structural distortions and show a direct-to-indirect bandgap transition as the 3D perovskite lattice is thinned to a monolayer in **1-Tl**. This bandgap transition at the monolayer limit is also evident in the calculations for **1-In**, an isostructural, isoelectronic analogue to **1-Tl** in which In^{3+} replaces Tl^{3+}, underscoring the orbital basis for the direct/indirect nature of the bandgap. Thus, in complement to the massive compositional diversity of halide double perovskites, dimensional reduction may be used as a systematic route for harnessing electronic confinement effects and obtaining new electronic structures.

Received 17th March 2020
Accepted 3rd June 2020

DOI: 10.1039/d0sc01580f

rsc.li/chemical-science

1. Introduction

In recent years, double perovskites have risen to the forefront of synthetic efforts in halide perovskites, driven in part by the substitutional flexibility of this family of materials. The $A_2BB'X_6$ (A = 1+ cation, X = halide) double perovskite structure splits the charge of the 2+ octahedral B-site metal present in ABX_3 single perovskites between two distinct octahedral sites, accommodating cations with charges from 1+ to 4+. This increased flexibility has afforded a class of materials with an astonishing array of optoelectronic properties. Exhibiting bandgaps large[1,2] and small,[3–6] direct[7,8] and indirect,[9–12] symmetry-allowed and symmetry-forbidden,[5,13,14] double perovskite band structures demonstrate how a diverse range of properties can arise from substitutions at a single atomic site.

Dimensional reduction[15] of the 3D double perovskite lattice to create lower-dimensional hybrid analogues offers yet more fertile ground for exploration. Indeed, studies performed since the 1990s have shown that dimensional reduction dramatically tunes the electronic structure in lead- and tin-halide single perovskites.[16–18] However, although double perovskites constitute a larger family of materials, known since the late 1800s,[19] the effects of dimensional reduction have not yet been elucidated. We recently probed the effects of dimensional confinement on halide double perovskites by synthesizing 2D derivatives of 3D $Cs_2AgBiBr_6$.[20] Unexpectedly, however, the optical properties of the layered double perovskites with monolayer- (n = 1, $(BA)_4AgBiBr_8$; BA = butylammonium, **1-Bi**) and bilayer-thick (n = 2, $(BA)_2CsAgBiBr_7$; **2-Bi**) inorganic sheets were strikingly similar. This is in stark contrast to the well-studied Pb and Sn single perovskites, whose optical properties show a large and systematic variation with n.[18,21–23] Indeed, even nanoparticles of the Ag–Bi perovskites[24,25] have not displayed the dramatic effects of quantum confinement seen in Pb-perovskite nanoparticles.[26,27]

It is important to determine if the minimal effect of quantum confinement observed in **1-Bi** and **2-Bi** is a general feature of 2D

[a]*Department of Chemistry, Stanford University, Stanford, California 94305, USA. E-mail: hemamala@stanford.edu*

[b]*Institute of Physics, University of Bayreuth, 95440 Bayreuth, Germany. E-mail: l.leppert@utwente.nl*

[c]*Stanford Institute for Materials and Energy Sciences, SLAC National Accelerator Laboratory, Menlo Park, California 94025, USA*

† Electronic supplementary information (ESI) available. The CIFs for **1-In**, **1-Tl**, **1'-Tl**, and **2-Tl_{PEA}** have been deposited in the CCDC 1943974–1943977, respectively. For ESI and crystallographic data in CIF or other electronic format see DOI: 10.1039/d0sc01580f

halide double perovskites, or whether it is specific to this Ag–Bi composition. However, the dearth of known 2D halide double perovskites does not allow us to answer this question. Prior to preparation of this manuscript only two other B-site combinations, Au^{I}–Au^{III} (ref. 28) and Cu^{I}–Bi^{III},[29] were known for this structure type (a third (Ag^{I}–In^{III}) was recently reported[30]). In the Au^{I}–Au^{III} perovskites, I_3^- coordination to Au is thought to perturb the electronic structure relative to the 3D analogues,[28] while in the case of the Cu^{I}–Bi^{III} composition, there is no 3D analogue for comparison.[29] Thus, neither family allows us to study the optoelectronic effects of dimensional reduction.

To reveal the optical and electronic effects of dimensional confinement in double perovskites, we focused on a composition with a delocalized electronic structure, $Cs_2AgTlBr_6$, featuring an unusually small bandgap (0.95 eV) and large band dispersion.[5] Herein, we present the effects of dimensional reduction on the optoelectronic properties of $Cs_2AgTlBr_6$ through the synthesis of a family of new double perovskites: two 2D $n = 2$ perovskites ($(A)_2CsAgTlBr_7$; A = phenethylammonium (PEA), **2-Tl$_{PEA}$** and A = butylammonium (BA), **2-Tl$_{BA}$**), a 2D $n = 1$ perovskite ($(3\text{-BPA})_4AgTlBr_8$; 3-BPA = 3-bromopropylammonium, **1-Tl**), and a quasi-1D $n = 1$ perovskite ($(HIS)_2AgTlBr_8$; HIS = histammonium, **1′-Tl**). We also synthesized the $n = 1$ Ag–In double perovskite ($(3\text{-BPA})_4AgInBr_8$, **1-In**) as an isoelectronic and isostructural analogue to **1-Tl**. Although the Ag–Tl and Ag–In layered perovskites are structurally similar to their Ag–Bi analogues, even showing similar metal coordination environments, their optical and electronic properties differ significantly. We characterize the optical properties of the Ag–Bi and Ag–Tl perovskites through ellipsometry. Whereas quantum confinement has a minimal impact on the optical properties of the layered Ag–Bi perovskites, we observe substantial optical changes upon dimensional reduction of the Ag–Tl materials, making this the first demonstration of clear optical changes induced by electronic confinement in lower-dimensional halide double perovskites. Importantly, our ellipsometry measurements allow us to trace the origin of the difference in optical behavior between the Ag–Tl and Ag–Bi perovskites to the more delocalized electronic character of the Ag–Tl materials. Finally, using density functional theory (DFT), we further explore direct-to-indirect gap transitions that occur in Ag–Tl and Ag–In perovskites when the 3D parent lattice is thinned to a monolayer at the $n = 1$ limit.

2. Results and discussion

2.1. Structure

2.1.1. Perovskite structure. The inorganic lattice of halide perovskites consists of a network of corner sharing metal-halide octahedra. In the 3D ABX_3 perovskites, the network of BX_6^{4-} octahedra extends infinitely along all three lattice vectors, and small monovalent A-site cations fill the cavities between octahedra (Fig. 1A). Using larger organic cations at the A sites partitions this 3D lattice into lower-dimensional derivatives (Fig. 1B and C). Here, organic layers partition the 3D inorganic network into 2D slabs, where the number of layers of metal-halide octahedra within the slabs (n) can be tuned by varying the ratio of small to large A-site cations. Commonly, the inorganic slabs of these structures correspond to slices taken along the (001) lattice plane of the 3D structure and have the general formula $A_2'A_{n-1}B_nX_{3n+1}$ (A = cation in the inorganic layer, A′ = cation in the organic layer). Within this family of (001) perovskites, the dimensionality of the inorganic lattice can be reduced to a single monolayer (the $n = 1$ structure, Fig. 1C).[31]

In the 3D rock-salt halide double perovskite (or elpasolite) structure, the divalent B-site cations of the ABX_3 structure are replaced by an ordered arrangement of two different B-site cations yielding the general formula $A_2BB'X_6$. Recently, renewed interest in these materials has greatly expanded the structural and electronic diversity of the perovskite family.[5,7,8,10–12,32] However, lower-dimensional analogues of elpasolites remain rare.[20,28–30,33] Seeking to expand the diversity of lower-dimensional double perovskites to better understand their optoelectronic properties, we synthesized several dimensionally reduced derivatives of $Cs_2AgTlBr_6$ and of the

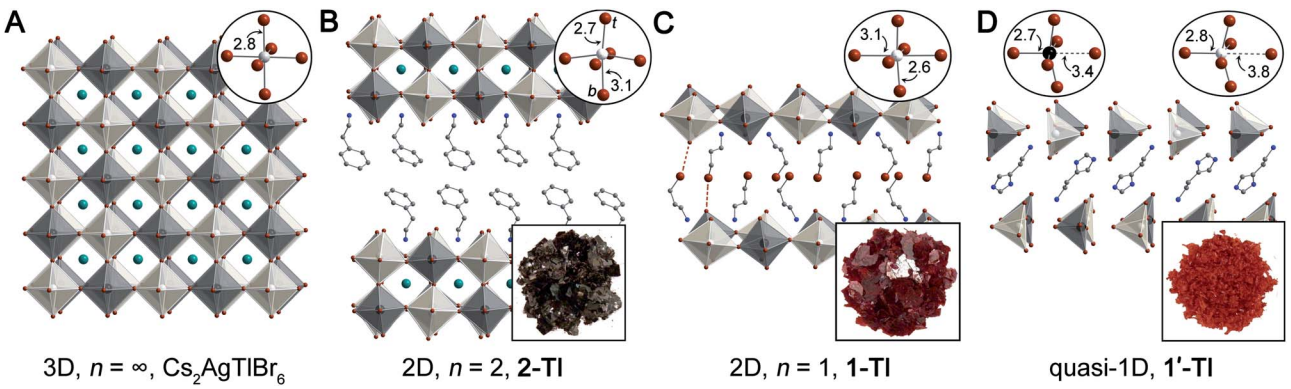

Fig. 1 Single-crystal X-ray diffraction structures of (A) $Cs_2AgTlBr_6$ (ref. 5) and three new lower-dimensional derivatives: (B) $(PEA)_2CsAgTlBr_7$ (**2-Tl$_{PEA}$**; PEA = phenethylammonium), (C) $(3\text{-BPA})_4AgBiBr_8$ (**1-Tl**; 3-BPA = 3-bromopropylammonium) with dotted lines showing Br···Br interactions, and (D) $(HIS)_2AgTlBr_8$ (**1′-Tl**; HIS = histammonium). Top insets show the metal coordination spheres (t = terminal, b = bridging) and bottom insets show the colors of the crystals. Black, white, teal, brown, blue, and gray spheres represent Tl, Ag, Cs, Br, N, and C atoms, respectively. H and disordered atoms omitted for clarity.

isoelectronic but unreported $Cs_2AgInBr_6$. See the ESI† for synthetic details and materials characterization.

2.1.2. $n = 1$ $(3\text{-BPA})_4AgTlBr_8$ (1-Tl). The single-crystal X-ray diffraction (SCXRD) structure of **1-Tl** is analogous to that of $(BA)_4AgBiBr_8$ (**1-Bi**, Table S3†).[20] Corner-sharing metal–bromide octahedra form 2D sheets with Ag^+ and Tl^{3+} cations alternating at the B sites, while bilayers of 3-BPA cations separate the inorganic slabs (Fig. 1C). In addition to the hydrogen bonding interactions of the ammonium cations with the inorganic lattice, we find short C–Br···Br–B contacts (3.7301(1) Å and 3.7889(1) Å for B = Tl^{3+} and Ag^+, respectively). These contacts are less than twice the van der Waals radius of Br (3.9 Å),[34] suggesting a weak interaction between the organo–bromines and the inorganic bromides (Fig. 1C). Such halogen–halogen interactions are known to stabilize 2D halide perovskites.[35–38] Crystals of $n = 1$ Ag–Tl perovskites synthesized using amines incapable of participating in such an interaction (*i.e.*, BA and PEA) were too disordered for structure determination through SCXRD, suggesting the important role of this weak Br···Br interaction in directing crystallization.

As is frequently observed for d^{10} transition metal centers,[39] the Ag–Br octahedra of **1-Tl** display an axial compression, with two short terminal Ag–Br bonds (2.5665(1) Å) perpendicular to the plane of the sheets and four long bridging Ag–Br bonds (3.0576(1) Å and 3.1421(1) Å) parallel to the plane of the sheet (Fig. 1C, inset). This distortion is analogous to that observed in **1-Bi**,[20] though larger in magnitude (Table S3†).

2.1.3. $n = 2$ $A_2CsAgTlBr_7$; A = PEA (2-Tl_{PEA}) or BA (2-Tl_{BA}). SCXRD reveals an $n = 2$ (001) perovskite structure for **2-Tl_{PEA}**. Here, the inorganic slabs are two octahedral layers thick, with Cs cations filling the cuboctahedral cavities within the inorganic sheets and PEA cations separating the sheets (Fig. 1B). The Ag^+ cations protrude outward from the plane of the inorganic sheet, forming a short bond with the terminal axial Br (2.6966(1) Å) and a long bond with the bridging axial Br (3.0502(1) Å) (Fig. 1B, inset), similar to the distortion of the Ag^+ site observed in $n = 2$ $(BA)_2CsAgBiBr_7$ (**2-Bi**; Table S4†).[20] Although we could not obtain a high-quality SCXRD solution for **2-Tl_{BA}**, powder X-ray diffraction (PXRD) data and elemental analysis indicate a structure similar to **2-Tl_{PEA}** and **2-Bi** (see ESI†).

2.1.4. $n = 1$ quasi-1D $(HIS)_2AgTlBr_8$ (1′-Tl). We decreased the dimensionality of the inorganic lattice of **1-Tl** by using the bulkier HIS cation to template the perovskite structure. SCXRD analysis afforded a structure similar to that of **1-Tl**. However, likely due to the bulky imidazolium ring of HIS, the Ag^+ and Tl^{3+} coordination environments are significantly distorted from octahedral symmetry, adopting a puckered shape where each B site forms five standard metal–bromide bonds and a sixth abnormally long metal–bromide contact (Fig. 1D, insets). These long metal–bromide contacts all point in the same direction and thus, the connectivity of the inorganic lattice resembles a series of 1D chains lying in a 2D plane (Fig. 1D). Here, the Ag–Br and Tl–Br bond lengths lying along the axis of these chains (3.0628 and 2.7005 Å, respectively) are comparable to the equatorial bond lengths found in **1-Tl**. In contrast, the long Ag–Br and Tl–Br contacts (3.7870 and 3.3771 Å, respectively) that lie along the direction perpendicular to the chain axis represent 21% and 23% increases in bond length, respectively, relative to the longest equatorial bonds in **1-Tl**, leading to the quasi-1D structure.

The quasi-1D connectivity in **1′-Tl** induces an obvious optical effect evidenced by the substantial color difference between this material (red-orange, Fig. 1D) and **1-Tl** (maroon, Fig. 1C). We quantify this difference using thin-film transmission spectra which reveal a substantial blueshift (*ca.* 220 meV) of the spectrum of **1′-Tl** relative to that of **1-Tl** (Fig. 2B). Additionally, band structure calculations point to decreased electronic dimensionality in **1′-Tl** arising from its quasi-1D connectivity (section 2.4).

2.1.5. $n = 1$ $(3\text{-BPA})_4AgInBr_8$ (1-In). In contrast to **1-Tl** and **1-Bi**, which form maroon and yellow plate-like crystals, respectively, **1-In** forms colorless plates (Fig. 2B). This difference is reflected in the thin-film transmission spectrum of **1-In** which displays an optical absorption onset that is blueshifted by *ca.* 1.4 eV relative to that of **1-Tl** (Fig. 2B). However, structurally, these three materials are quite similar. The Ag–Br octahedra in **1-In** exhibit a similar (albeit slightly more pronounced) axial compression and maintain comparable angular distortions relative to **1-Tl** and **1-Bi** (Table S3†). As in **1-Tl**, we find relatively short C–Br···Br–B contacts in **1-In** (3.7634(2) and 3.8107(2) Å for B = In^{3+} and Ag^+, respectively), indicative of weak interaction between the organo-bromines and inorganic bromides. The structure of **1-In** is similar to that of the recently reported $(propylammonium)_4AgInBr_8$.[30]

Although $Cs_2AgInCl_6$ has been reported,[8] to date there are no reports of the successful synthesis of the bromide analogue. The octahedral tolerance factor (μ) of In^{3+} coordinated by six bromides suggests that $Cs_2AgInBr_6$ may be unstable.[8] The additional structural flexibility afforded by the 2D perovskite lattice diminishes the relevance of stability criteria like μ, explaining the isolation of **1-In**.

2.2. Contrasting optical properties of Ag^I–M^{III} layered perovskites (M = Tl, Bi)

2.2.1. Color and absorption spectra of the Ag–Tl and Ag–Bi perovskites. As discussed in sections 2.1.2 and 2.1.3, the structural distortions that accompany dimensional reduction

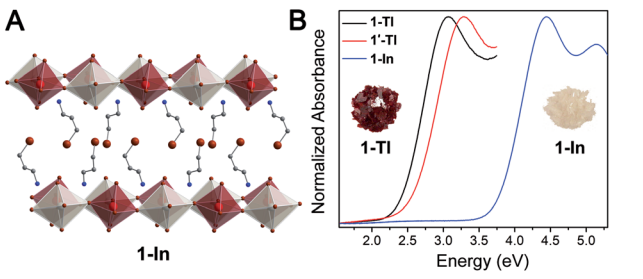

Fig. 2 (A) Single-crystal X-ray diffraction structure of $(3\text{-BPA})_4AgInBr_8$ (**1-In**). Dark red, white, brown, blue, and gray spheres represent In, Ag, Br, N, and C atoms, respectively. H and disordered atoms omitted for clarity. (B) Thin-film transmission spectra of **1-Tl** (black), **1′-Tl** (red), and **1-In** (blue) with crystals of **1-Tl** and **1-In** pictured in the insets.

are remarkably similar in the $n = 1$ and $n = 2$ Ag–Bi and Ag–Tl perovskites (Fig. S21†). However, the optical effects of dimensional reduction are strikingly different. In the Ag–Tl perovskites, increasing the n value leads to a significant color change from $n = 1$ **1-Tl**, which forms maroon crystals, to $n = 2$ **2-Tl$_{PEA/BA}$**, which forms black crystals (Fig. 3C). In contrast, crystals of **1-Bi** and **2-Bi** are nearly identical shades of yellow despite their different n values (Fig. 3A). Diffuse reflectance measurements of powders of **1-Tl**, **2-Tl$_{PEA/BA}$**, **1-Bi**, and **2-Bi** give absorption onsets consistent with this observation; a significantly larger redshift in absorption onset occurs moving from **1-Tl** to **2-Tl$_{PEA/BA}$** than when moving from **1-Bi** to **2-Bi** (Fig. S1†). It is important to note that, while these diffuse reflectance measurements allow us to qualitatively assess the absorption onset of these materials, we should not attempt to extract a quantitative value for their bandgaps from this data since diffuse reflectance is highly sensitive to weak absorption events which have many possible origins (see ESI† for a full discussion).

2.2.2. Single-crystal ellipsometry of the Ag–Tl and Ag–Bi perovskites. To further investigate the contrasting dependence of optical properties on the n value observed in the Ag–Bi and Ag–Tl perovskites, we probed the strong absorption events of these materials using ellipsometry (a technique which measures the change in polarization of light incident on a sample) to reliably extract optical constants from single crystals of **1-Tl**, **2-Tl$_{BA}$**, **1-Bi**, and **2-Bi**. These crystals grow as thin flat plates with the layers parallel to the face of the plate. Large (mm scale) single crystals with well-formed facets were selected for ellipsometry measurements, and the top surface was exfoliated using a rigid sticky surface exposing a highly reflective (001) face (see ESI† for details). Because ellipsometry employs polarized light and because our materials have anisotropic structures, several measurements were taken on each crystal, varying the orientation of the top surface with respect to the incident light beam (see ESI†). The plate-like morphology of the crystals precluded measurements where the light beam was incident on the thin edge of the crystal.

The variation of absorption coefficient (α) with photon energy obtained from ellipsometry measurements of crystals of **1-Tl**, **2-Tl$_{BA}$**, **1-Bi**, and **2-Bi** is shown in Fig. 3A and C. Notably, for **1-Bi** and **2-Bi**, the ellipsometry traces have very similar shapes to the thin-film transmission spectra, validating the use of ellipsometry as a probe of strong absorption events (Fig. 3B and S8†).[20] It is important to note that, because ellipsometry and thin-film transmission measurements are only sensitive to a material's strongest absorptions, the absorption onsets observed in these spectra do not necessarily correspond to the bandgap onset because weak absorption from indirect or symmetry-forbidden direct gaps (with absorption coefficients $<10^4$ cm^{-1}) are not evident.

For **1-Bi**, **2-Bi**, and **2-Tl$_{BA}$**, the ellipsometry spectra did not vary substantially as the crystal was rotated and only one representative trace is shown (see ESI†). In contrast, for **1-Tl**, the spectra obtained in different orientations differ significantly (Fig. S10†). We find that two distinct orientations of **1-Tl**, defined as 0° and 90°, give unique ellipsometry spectra represented by the traces **1-Tl$_0$** and **1-Tl$_{90}$** in Fig. 3C. The average of these unique spectra looks very similar to the thin-film transmission spectrum of **1-Tl** (Fig. 3D) consistent with the fact that the thin-film transmission measurement employs unpolarized light incident on a multi-crystalline thin film, where the in-plane unit-cell vectors are randomly oriented. The underlying electronic origin of the optical anisotropy in **1-Tl** is currently under investigation.

The ellipsometry spectra of the 2D Ag–Bi perovskites change very little with n. Both **1-Bi** and **2-Bi** display a narrow, isolated absorption feature at *ca.* 3.0 eV that shifts minimally (*ca.* 50 meV) between the two materials (Fig. 3A). Fits to the ellipsometry data yield essentially the same full width at half maximum (fwhm, 0.29 eV) for this transition in both $n = 1$ **1-Bi** and $n = 2$ **2-Bi** (see ESI†).

In contrast, the lowest-energy feature in the Ag–Tl perovskites shows a substantial dependence on n. The spectra of **1-Tl$_0$** and **2-Tl$_{BA}$** exhibit a lowest-energy absorption feature peaked at nearly the same energy (*ca.* 3.0 eV), though in both cases, the feature is substantially broader than the peak in **1-Bi** and **2-Bi** (Fig. 3C). Fits of these spectra indicate that the lowest-energy feature in **2-Tl$_{BA}$** is much broader than that of **1-Tl**. Using a series of Lorentzian-like oscillators to fit the spectra according

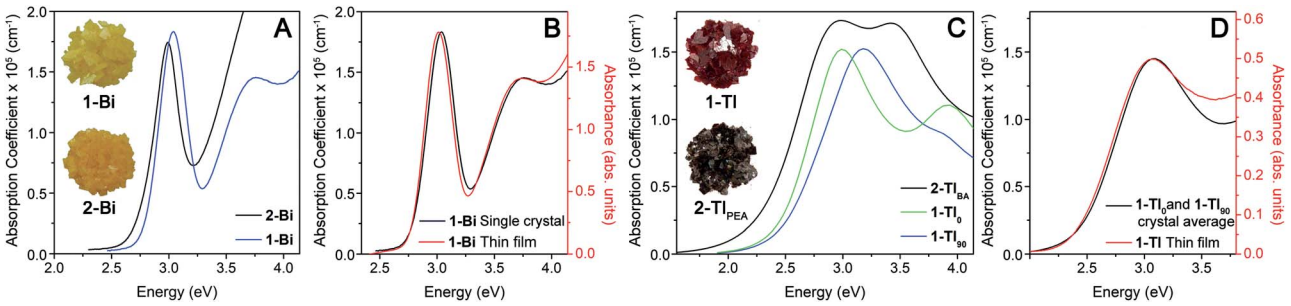

Fig. 3 (A) The absorption coefficient (*a*) of **1-Bi** (blue) and **2-Bi** (black) as a function of photon energy, extracted from single-crystal ellipsometry measurements. Inset: crystals of **1-Bi** and **2-Bi** showing a similar color. (B) Single-crystal ellipsometry data (black) and the thin-film transmission spectrum of **1-Bi** (red), demonstrating the similar results. (C) The α of **2-Tl$_{BA}$** (black) and **1-Tl** (blue and green) as a function of photon energy extracted from single-crystal ellipsometry measurements. The green and blue traces show the spectra of **1-Tl** for the two unique orientations defined as 0° (**1-Tl$_0$**) and 90° (**1-Tl$_{90}$**), respectively. Inset: crystals of **1-Tl** and **2-Tl** showing a clear color difference. (D) The average of the green and blue traces in C (black) and the thin-film transmission spectrum of **1-Tl** (red), showing their similarity.

to the new amorphous dispersion formula, we find a broadening parameter for the major oscillator describing this lowest-energy feature in **2-Tl$_{BA}$** that is *ca.* 41% larger than in the case of **1-Tl$_0$** and *ca.* 19% larger than in the case of **1-Tl$_{90}$** (see ESI†). Thus, in contrast to the 2D Ag–Bi perovskites whose optical spectra are essentially unaffected by n value, the optical spectra of the 2D Ag–Tl perovskites evolve substantially with changing n.

2.3. Contrasting electronic properties of Ag^{I}–M^{III} layered perovskites (M = Tl, Bi)

2.3.1. Electronic delocalization. The differences in optical properties between the Ag–Tl and Ag–Bi perovskites observed through ellipsometry point to a fundamental difference in their electronic structures. The relatively small fwhm of the lowest-energy absorption features in **1-Bi** and **2-Bi** and the invariance of the fwhm with changing dimensionality suggest that these peaks arise from highly localized molecule-like transitions. Localized states lead to flat electronic bands, and transitions between such states yield narrow optical absorption features. Furthermore, localized states do not interact significantly with the surrounding lattice and are thus insensitive to the effects of dimensional confinement. Previously, we proposed that the narrow absorption feature in **1-Bi** and **2-Bi** arises from a transition between Ag d/Br p and Bi p/Br p states in the relatively flat valence and conduction bands, respectively, implying significant metal-to-metal charge transfer (MMCT) character.[20]

The significantly greater width of the absorption features in the Ag–Tl perovskites and the larger influence of dimensionality on their breadth suggest greater electronic delocalization. Delocalized wavefunctions yield dispersive bands and give rise to broad optical transitions. In addition, quantum confinement forces increased localization of the wavefunction, leading to narrowing of absorption features and pronounced effects of dimensional reduction.

Our ellipsometry studies demonstrate the substantial effect of n value on the optical properties of the Ag–Tl perovskites, making this the first demonstration of clear quantum confinment effects in 2D double perovskites, and trace this observation to the delocalized electronic character of the Ag–Tl perovskites. Despite this, we do not observe any spectral signatures of excitonic behavior resembling those observed upon quantum confinement of the well-studied Pb perovskites. Sharp excitonic absorption features observed in 2D Pb perovskites through single-crystal reflectance spectroscopy,[40] ellipsometry,[41] and thin-film transmission spectroscopy[42] are absent in our materials. Indeed, clear excitonic features have not been seen in any composition of halide double perovskite to date. Additionally, although (001) Pb–Br perovskites show bright excitonic emission at room temperature,[43] neither **1-Tl**, **2-Tl$_{BA}$**, nor any other composition of low-dimensional halide double perovskite has shown excitonic photoluminescence to date. Thus, any excitonic states in these materials are expected to differ from those of the well-studied Pb perovskites.

2.3.2 Band composition. To understand the underlying reason for the large differences in optical properties of the Ag–Tl and Ag–Bi perovskites, we used DFT to compute the band structures of **1-Tl**, **2-Tl$_{PEA}$**, **1-Bi**, and **2-Bi** from the SCXRD structures (see ESI†). For **1-Bi** and **2-Bi** the band structures were calculated with the PBE exchange-correlation functional, including spin–orbit coupling self-consistently.[20] However, because the PBE functional predicts a negative bandgap for the small-bandgap $Cs_2AgTlBr_6$, we used the HSE06 exchange-correlation functional for the Ag–Tl perovskites. The valence band maximum (VBM) of the layered Ag–Bi perovskites is primarily composed of Ag d and Br p states, with an appreciable contribution from Bi s states only in the case of **2-Bi** (Fig. S22A and B†).[20] Similarly, the VBM in the layered Ag–Tl perovskites is composed primarily of Ag d and Br p states (Fig. 4C and D). In contrast, the composition of the conduction band (CB) differs greatly between the Ag–Bi and Ag–Tl perovskites. While Bi p and Br p orbital character predominates in the CB of the Ag–Bi perovskites (Fig. S22A and B†), Tl s and Br p character predominates in the CB of the Ag–Tl perovskites (Fig. 4C and D). (Although Ag s orbitals appear at the conduction band minimum (CBM) in **2-Bi** and **2-Tl$_{PEA}$**, these contributions are relatively minor.) This difference in CB composition likely leads to the optical differences between the Ag–Bi and Ag–Tl perovskites. The spherically symmetric, diffuse Tl s orbitals generate increased orbital interaction, which in turn, promotes increased electronic delocalization. This increased delocalization is evident in the significantly greater degree of band dispersion present in the CB of **1-Tl** and **2-Tl$_{PEA}$** relative to that of **1-Bi** and **2-Bi**, respectively (Fig. S22†).

2.4. Electronic effects of dimensional reduction

Previously, we found that the Ag–Bi double perovskites with $\infty \geq n > 1$ have an indirect bandgap between analogous k-points. This band structure changed significantly at the $n = 1$ limit, affording a direct bandgap.[20] This indirect-to-direct gap transition is reminiscent of the effects of exfoliating bulk MoS_2 to individual layers.[44,45] Although $Cs_2AgTlBr_6$ (ref. 5) is electronically distinct from $Cs_2AgBiBr_6$,[11,12] we see a similar bandgap transition upon dimensional reduction. Consistent with prior work,[5] we find that 3D $Cs_2AgTlBr_6$ has a direct bandgap at the Γ point with a valence band maximum (VBM) composed entirely of Ag d and Br p orbitals and a conduction band minimum (CBM) composed mainly of Tl s and Br p orbitals with a smaller contribution from Ag s orbitals (Fig. 4A). The band structure of **2-Tl$_{PEA}$** is analogous to that of the parent 3D material; we find a direct bandgap at the Γ point and similar orbital make-up of the VBM and CBM (Fig. 4C). The similar shape of the band dispersion in the band structures of $Cs_2AgTlBr_6$ (plotting the X → L → Γ path) and **2-Tl$_{PEA}$** (plotting the analogous V → X → Γ path, see ESI†) further highlights the analogy between the electronic structures of the 3D perovskite and its $n = 2$ derivative. Nevertheless, a distinguishing feature of the band structure of **2-Tl$_{PEA}$** is the lack of band dispersion along the layer stacking direction (Γ → Z) which reflects the electronically 2D nature of this material (Fig. S25†). We also constructed a model $n = 3$ system by relaxing the structure of an $n = 3$ slab cut from the 3D

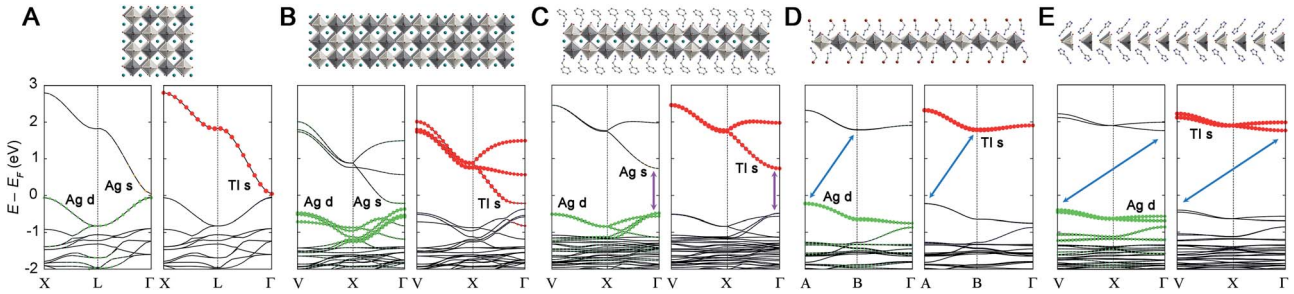

Fig. 4 Structures (top) and electronic band structures (bottom) of (A) $Cs_2AgTlBr_6$, (B) an $n = 3$ Ag–Tl structure, (C) **2-Tl$_{PEA}$**, (D) **1-Tl**, and (E) **1′-Tl**. A model structure was used in B ($n = 3$), all other structures are from SCXRD. Analogous k-paths are plotted in all panels to demonstrate the decrease in band dispersion with dimensional reduction and to highlight the abrupt change in band structure at the $n = 1$ limit. A–C show direct gaps at Γ (purple arrows in C) whereas an indirect gap is evident in D and E (blue arrows). White, black, brown, teal, blue, and gray spheres represent Ag, Tl, Br, Cs, N, and C atoms, respectively. Band structures are shown in duplicate with Ag and Tl orbital contributions denoted by the size of the colored circles in the left and right panels, respectively. Halide orbital contributions are present throughout, but not shown for clarity.

material (see ESI†). The band structure of this model $n = 3$ system shows the same close analogy to the 3D band structure as **2-Tl$_{PEA}$** (Fig. 4B). This suggests that all Ag–Tl double perovskites with $n \geq 2$ have analogous band structures.

Interestingly, further dimensional reduction of the Ag–Tl perovskite lattice to the $n = 1$ limit yields substantial changes in band structure. The band structure of **1-Tl** reveals an indirect gap between the A point in the VB and the B point in the CB (Fig. 4D). Additionally, the Ag s-orbital contribution is greatly reduced in the CB and the bandgap transition becomes an almost pure Ag-to-Tl MMCT. Once again, we find no dispersion along the layer stacking direction (Γ → Z) in **1-Tl**, evidencing its electronically 2D nature (Fig. S25†).

Structural distortions of the inorganic lattice can significantly affect band dispersion and therefore, the direct/indirect nature of the bandgap.[20] To separate the effects of dimensional reduction and the accompanying structural distortion, we constructed model $n = 1$ and 2 Ag–Tl materials (**1M** and **2M**, respectively) with bond lengths and angles identical to those found in the cubic 3D structure (see ESI†). We find that the band structure of **2M** (Fig. S23D†) retains a direct bandgap at Γ, and the band structure of **1M** retains an indirect bandgap, although here, the CBM shifts from B to Γ (Fig. S23B†). This result indicates that the direct-to-indirect bandgap transition observed when moving from $Cs_2AgTlBr_6$ to **1-Tl** is driven by dimensional reduction.

To further probe this direct-to-indirect bandgap transition at the $n = 1$ limit, we calculated the band structure of the isoelectronic $n = 1$ perovskite **1-In** using the SCXRD structure. This material has an orbital makeup analogous to **1-Tl** with s-orbital character in the CB. However, due to the significantly higher energy of the In 5s orbitals relative to the Tl 6s orbitals, the CB shifts up in energy and we calculate a 1.3 eV larger bandgap for **1-In** than for **1-Tl** (Table S7†), consistent with our experimental observation of a *ca.* 1.4 eV blueshifted absorption onset in **1-In** (Fig. 2B). Calculations still predict a direct-to-indirect bandgap transition when the 3D Ag–In parent lattice is thinned to a monolayer; our calculations show an indirect bandgap in **1-In**, consistent with a recent calculation for an analogous structure.[30] The indirect gap in **1-In** occurs between the A point in the VB and the Γ point in the CB (Fig. S24†), analogous to **1M**, whereas a direct bandgap has been reported at the Γ point for the 3D analogue $Cs_2AgInCl_6$.[8] This finding highlights the significance of orbital symmetry in dictating the direct/indirect nature of the bandgap in both 3D double perovskites[46,47] and their layered derivatives.

Despite the significant structural distortions of the inorganic lattice of **1′-Tl**, this quasi-1D structure retains an indirect bandgap similar to that of the less distorted 2D **1-Tl** (Fig. 4E). However, we find substantially less band dispersion in **1′-Tl**, consistent with lower dimensionality caused by increased structural distortion of the inorganic lattice.

3. Conclusion

We report several new lower-dimensional analogues of the 3D double perovskite $Cs_2AgTlBr_6$. The $n = 1$ and $n = 2$ 2D perovskites, **1-Tl** and **2-Tl$_{PEA/BA}$**, are structurally similar to the analogous Ag–Bi perovskites (**1-Bi** and **2-Bi**) (Fig. S21†). In **1′-Tl**, structural distortions produce a lattice with quasi-1D connectivity. Unlike the $n = 1$ (**1-Bi**) and 2 (**2-Bi**) layered derivatives of 3D $Cs_2AgBiBr_6$, which are a similar shade of yellow, the lower-dimensional derivatives of 3D $Cs_2AgTlBr_6$ show significantly different colors for the 2D $n = 2$ (**2-Tl$_{PEA/BA}$**; black) and $n = 1$ (**1-Tl**; maroon) members and the quasi-1D structure (**1′-Tl**; red-orange). Single-crystal ellipsometry measurements underscore this difference. In the Ag–Bi perovskites, the strong low-energy absorption is dominated by narrow features that change very little as n varies, suggesting localized molecule-like character. In contrast, much broader features with a stronger dependence on n dominate in the Ag–Tl analogues, suggesting delocalized electronic character that is more sensitive to quantum confinement. We attribute this difference to the replacement of Bi 6p orbitals in the CB of the Ag–Bi perovskites with diffuse, spherically symmetric Tl 6s orbitals in the CB of the Ag–Tl perovskites, which promotes enhanced orbital interaction leading to greater electronic delocalization.

We also find that all members of the Ag–Tl perovskite family with $n \geq 2$ have analogous band structures, exhibiting direct

bandgaps. In contrast, the band structure of $n = 1$ **1-Tl** displays significant differences, most notably, an indirect bandgap. This indirect bandgap is retained in **1′-Tl** despite the quasi-1D connectivity of the inorganic lattice. Importantly, using calculations on undistorted model structures, we find that this direct-to-indirect bandgap transition is driven by dimensional reduction rather than by the accompanying structural distortions of the lattice. We also synthesize **1-In** as an isoelectronic, isostructural analogue of **1-Tl**. Despite the higher energy of the CB in the Ag–In perovskites, calculations show a similar direct-to-indirect bandgap transition, demonstrating that the analogous symmetry of the bands preserves the change in electronic structure upon dimensional reduction. Our studies of dimensional reduction of 3D halide double perovskites so far have revealed an indirect-to-direct bandgap transition at the $n = 1$ limit of $Cs_2AgBiBr_6$ (ref. 20) and a direct-to-indirect bandgap transition at the $n = 1$ limit of $Cs_2AgTlBr_6$. This substantial change in band structure observed at the inorganic monolayer limit in two electronically distinct double perovskites is intriguing and understanding the generality of this phenomenon warrants further study.

Electronic confinement effects in Pb-halide single perovskites have yielded widely varying phenomena, generating materials with applications ranging from solar-cell absorbers with high open-circuit voltages[48] to phosphors with emissions ranging from the visible to the near-IR.[27,49] This work shows that tuning the dimensionality of the inorganic sublattice can also afford significant changes in the optoelectronic properties of the much larger family of halide double perovskites, particularly when the parent 3D double perovskite has substantial electronic delocalization.

Conflicts of interest

There are no conflicts to declare.

Acknowledgements

This work is supported by the Department of Energy, Office of Science, Basic Energy Sciences (DOE, BES), Division of Materials Sciences and Engineering under Contract DE-AC02-76SF00515. SC-XRD studies were performed at beamlines 11.3.1 and 12.2.1 at the Advanced Light Source (ALS) at the Lawrence Berkeley National Laboratory and at the Stanford Nano Shared Facilities, supported by the National Science Foundation (ECCS-1542152). B. A. C. is supported by an NSF graduate fellowship (DGE-114747). R. I. B. and L. L. acknowledge support by the Bavarian State Ministry of Science, Research, and the Arts through the grant "Solar Technologies go Hybrid", the Elite Network Bavaria, the German Research Foundation through SFB840, and computational resources provided by the Bavarian Polymer Institute. Work at the ALS was supported by the DOE, BES (DE-AC02-05CH11231). We thank A. H. Slavney for helpful discussions and Dr S. J. Teat for crystallographic advice.

Notes and references

1 F. Pelle, B. Jacquier, J. P. Denis and B. Blanzat, *J. Lumin.*, 1978, **17**, 61–72.
2 P. S. Bryan and S. A. Ferranti, *J. Lumin.*, 1984, **31–32**, 117–119.
3 H. L. Wells, *Am. J. Sci.*, 1922, **3**, 315–326.
4 V. Auger and T. Karantassis, *C. R. Hebd. Seances Acad. Sci.*, 1925, **180**, 1845–1847.
5 A. H. Slavney, L. Leppert, A. Saldivar Valdes, D. Bartesaghi, T. J. Savenije, J. B. Neaton and H. I. Karunadasa, *Angew. Chem., Int. Ed.*, 2018, **57**, 12765–12770.
6 M.-G. Ju, M. Chen, Y. Zhou, H. F. Garces, J. Dai, L. Ma, N. P. Padture and X. C. Zeng, *ACS Energy Lett.*, 2018, **3**, 297–304.
7 Z. Deng, F. Wei, S. Sun, G. Kieslich, A. K. Cheetham and P. D. Bristowe, *J. Mater. Chem. A*, 2016, **4**, 12025–12029.
8 G. Volonakis, A. A. Haghighirad, R. L. Milot, W. H. Sio, M. R. Filip, B. Wenger, M. B. Johnston, L. M. Herz, H. J. Snaith and F. Giustino, *J. Phys. Chem. Lett.*, 2017, **8**, 772–778.
9 M. Retuerto, T. Emge, J. Hadermann, P. W. Stephens, M. R. Li, Z. P. Yin, M. Croft, A. Ignatov, S. J. Zhang, Z. Yuan, C. Jin, J. W. Simonson, M. C. Aronson, A. Pan, D. N. Basov, G. Kotliar and M. Greenblatt, *Chem. Mater.*, 2013, **25**, 4071–4079.
10 A. H. Slavney, T. Hu, A. M. Lindenberg and H. I. Karunadasa, *J. Am. Chem. Soc.*, 2016, **138**, 2138–2141.
11 E. T. McClure, M. R. Ball, W. Windl and P. M. Woodward, *Chem. Mater.*, 2016, **28**, 1348–1354.
12 M. R. Filip, S. Hillman, A. A. Haghighirad, H. J. Snaith and F. Giustino, *J. Phys. Chem. Lett.*, 2016, **7**, 2579–2585.
13 A. E. Maughan, A. M. Ganose, M. M. Bordelon, E. M. Miller, D. O. Scanlon and J. R. Neilson, *J. Am. Chem. Soc.*, 2016, **138**, 8453–8464.
14 W. Meng, X. Wang, Z. Xiao, J. Wang, D. B. Mitzi and Y. Yan, *J. Phys. Chem. Lett.*, 2017, **8**, 2999–3007.
15 E. G. Tulsky and J. R. Long, *Chem. Mater.*, 2001, **13**, 1149–1166.
16 X. Hong, T. Ishihara and A. V. Nurmikko, *Solid State Commun.*, 1992, **84**, 657–661.
17 C. C. Stoumpos, D. H. Cao, D. J. Clark, J. Young, J. M. Rondinelli, J. I. Jang, J. T. Hupp and M. G. Kanatzidis, *Chem. Mater.*, 2016, **28**, 2852–2867.
18 D. B. Mitzi, C. A. Feild, W. T. A. Harrison and A. M. Guloy, *Nature*, 1994, **369**, 467–469.
19 C. W. Cross and W. F. Hillebrand, *Am. J. Sci.*, 1883, **26**, 271–294.
20 B. A. Connor, L. Leppert, M. D. Smith, J. B. Neaton and H. I. Karunadasa, *J. Am. Chem. Soc.*, 2018, **140**, 5235–5240.
21 J. Calabrese, N. L. Jones, R. L. Harlow, N. Herron, D. L. Thorn and Y. Wang, *J. Am. Chem. Soc.*, 1991, **113**, 2328–2330.
22 X. Hong, T. Ishihara and A. V. Nurmikko, *Phys. Rev. B*, 1992, **45**, 6961–6964.
23 D. B. Mitzi, S. Wang, C. A. Feild, C. A. Chess and A. M. Guloy, *Science*, 1995, **267**, 1473–1476.
24 S. E. Creutz, E. N. Crites, M. C. De Siena and D. R. Gamelin, *Nano Lett.*, 2018, **18**, 1118–1123.

25 Y. Bekenstein, J. C. Dahl, J. Huang, W. T. Osowiecki, J. K. Swabeck, E. M. Chan, P. Yang and A. P. Alivisatos, *Nano Lett.*, 2018, **18**, 3502–3508.
26 L. C. Schmidt, A. Pertegás, S. González-Carrero, O. Malinkiewicz, S. Agouram, G. M. Espallargas, H. J. Bolink, R. E. Galian and J. Pérez-Prieto, *J. Am. Chem. Soc.*, 2014, **136**, 850–853.
27 L. Protesescu, S. Yakunin, M. I. Bodnarchuk, F. Krieg, R. Caputo, C. H. Hendon, R. X. Yang, A. Walsh and M. V. Kovalenko, *Nano Lett.*, 2015, **15**, 3692–3696.
28 L. M. Castro-Castro and A. M. Guloy, *Angew. Chem., Int. Ed.*, 2003, **42**, 2771–2774.
29 L.-Y. Bi, Y.-Q. Hu, M.-Q. Li, T.-L. Hu, H.-L. Zhang, X.-T. Yin, W.-X. Que, M. S. Lassoued and Y.-Z. Zheng, *J. Mater. Chem. A*, 2019, **7**, 19662–19667.
30 L. Mao, S. M. L. Teicher, C. C. Stoumpos, R. M. Kennard, R. A. DeCrescent, G. Wu, J. A. Schuller, M. L. Chabinyc, A. K. Cheetham and R. Seshadri, *J. Am. Chem. Soc.*, 2019, **141**, 19099–19109.
31 D. B. Mitzi, *J. Chem. Soc., Dalton Trans.*, 2001, 1–12.
32 F. Wei, Z. Deng, S. Sun, F. Xie, G. Kieslich, D. M. Evans, M. A. Carpenter, P. D. Bristowe and A. K. Cheetham, *Mater. Horiz.*, 2016, **3**, 328–332.
33 M. K. Jana, S. M. Janke, D. J. Dirkes, S. Dovletgeldi, C. Liu, X. Qin, K. Gundogdu, W. You, V. Blum and D. B. Mitzi, *J. Am. Chem. Soc.*, 2019, **141**, 7955–7964.
34 L. Pauling, in *The Nature of the Chemical Bond and the Structure of Molecules and Crystals: An Introduction to Modern Structural Chemistry*, Cornell University Press, Ithaca, New York, 3 edn, 1960, ch. 7, pp. 257–264.
35 A. Lemmerer and D. G. Billing, *CrystEngComm*, 2010, **12**, 1290–1301.
36 M. D. Smith, L. Pedesseau, M. Kepenekian, I. C. Smith, C. Katan, J. Even and H. I. Karunadasa, *Chem. Sci.*, 2017, **8**, 1960–1968.
37 V. Gómez, O. Fuhr and M. Ruben, *CrystEngComm*, 2016, **18**, 8207–8219.
38 S. Sourisseau, N. Louvain, W. Bi, N. Mercier, D. Rondeau, F. Boucher, J.-Y. Buzaré and C. Legein, *Chem. Mater.*, 2007, **19**, 600–607.
39 L. E. Orgel, *J. Chem. Soc.*, 1958, 4186–4190, DOI: 10.1039/JR9580004186.
40 T. Ishihara, J. Takahashi and T. Goto, *Solid State Commun.*, 1989, **69**, 933–936.
41 S. Zhang, P. Audebert, Y. Wei, A. Al Choueiry, G. Lanty, A. Bréhier, L. Galmiche, G. Clavier, C. Boissière, J.-S. Lauret and E. Deleporte, *Materials*, 2010, **3**, 3385–3406.
42 C.-q. Xu, S. Fukuta, H. Sakakura, T. Kondo, R. Ito, Y. Takahashi and K. Kumata, *Solid State Commun.*, 1991, **77**, 923–926.
43 K. Tanaka, T. Takahashi, T. Kondo, K. Umeda, K. Ema, T. Umebayashi, K. Asai, K. Uchida and N. Miura, *Jpn. J. Appl. Phys.*, 2005, **44**, 5923–5932.
44 A. Splendiani, L. Sun, Y. Zhang, T. Li, J. Kim, C.-Y. Chim, G. Galli and F. Wang, *Nano Lett.*, 2010, **10**, 1271–1275.
45 K. F. Mak, C. Lee, J. Hone, J. Shan and T. F. Heinz, *Phys. Rev. Lett.*, 2010, **105**, 136805.
46 A. H. Slavney, B. A. Connor, L. Leppert and H. I. Karunadasa, *Chem. Sci.*, 2019, **10**, 11041–11053.
47 T. T. Tran, J. R. Panella, J. R. Chamorro, J. R. Morey and T. M. McQueen, *Mater. Horiz.*, 2017, **4**, 688–693.
48 I. C. Smith, E. T. Hoke, D. Solis-Ibarra, M. D. McGehee and H. I. Karunadasa, *Angew. Chem., Int. Ed.*, 2014, **53**, 11232–11235.
49 M. D. Smith, B. A. Connor and H. I. Karunadasa, *Chem. Rev.*, 2019, **119**, 3104–3139.